Pedestrian Flow Models with Slowdown Interactions

A. CHERTOCK   A. KURGANOV
A. POLIZZI   I. TIMOFEYEV

Pedestrian Flow Models with Slowdown Interactions

Alina Chertock[*], Alexander Kurganov[†], Anthony Polizzi[‡], and Ilya Timofeyev[§]

Abstract

In this paper, we introduce and study one-dimensional models for the behavior of pedestrians in a narrow street or corridor. We begin at the microscopic level by formulating a stochastic cellular automata model with explicit rules for pedestrians moving in two opposite directions. Coarse-grained mesoscopic and macroscopic analogs are derived leading to the coupled system of PDEs for the density of the pedestrian traffic. The obtained first-order system of conservation laws is only conditionally of hyperbolic. We also derive higher-order nonlinear diffusive corrections resulting in a parabolic macroscopic PDE model. We perform numerical experiments, which compare and contrast the behavior of the microscopic stochastic model and the resulting coarse-grained PDEs for various parameter settings and initial conditions. We also demonstrate that the nonlinear diffusion is essential for reproducing the behavior of the stochastic system in the nonhyperbolic regime.

1 Introduction

In contrast with the considerable effort devoted to the modeling of vehicular traffic, modeling of pedestrian traffic received little attention until fairly recently. In the past two decades, a variety of pedestrian traffic and crowd dynamics models have been proposed, ranging from agent-based microscopic to macroscopic PDE models describing various phenomena such as crowd behavior under panic, pedestrian planning, structural design, etc., see [3,13,15] and the review papers [4,14] for examples and references.

Cellular automata (CA) has a long history of applications in different areas of science and engineering. In particular, the CA models have been applied to the vehicular traffic to derive a coarse-grained PDE description with the look-ahead dynamics for the density of the car traffic [21]. Multilane and multiclass were also considered as extensions of the original model [1,7,8,22]. CA microscopic models with empirical rules have also been used to simulate pedestrian movement [5,6,9,11].

The main emphasis of the present work is on the connection between the microscopic CA models for the bi-directional pedestrian traffic and its coarse-grained PDE analogs. In particular, this paper illustrates how microscopic interaction rules can be coarse-grained and are manifested in a macroscopic PDE model. In addition, we also derive a nonlinear second-order diffusive correction

---

[*]Department of Mathematics, North Carolina State University, Raleigh, NC 27695, USA; chertock@math.ncsu.edu

[†]Mathematics Department, Tulane University, New Orleans, LA 70118, USA; kurganov@math.tulane.edu

[‡]Mathematics Department, Tulane University, New Orleans, LA 70118, USA; apolizz@tulane.edu

[§]Department of Mathematics, University of Houston, Houston, TX 77204, USA; ilya@math.uh.edu

of the obtained first-order PDE model. These diffusive terms are derived systematically and can be used in other models of pedestrian traffic instead of an approach where diffusive terms are often added to the right-hand side in an ad-hoc fashion. Another mathematical question which is addressed in this paper is the validity of the approximate independence assumption. This assumption is commonly used in the derivation of various coarse-grained PDE models from their microscopic CA formulation. We demonstrate that the strength of interactions weakly affects the independence assumption and, ultimately, leads to the break down of the coarse-grained derivation. Nevertheless, our simulations show that the coarse-grained PDE model is valid for a wide range of parameters. Moreover, we also demonstrate that the nonlinear diffusion is essential for reproducing the behavior of the microscopic model in some regimes.

We utilize the CA approach to formulate a one-dimensional (1-D) microscopic model for the pedestrian motion in a narrow street of corridor and derive a corresponding PDE description for the density of the pedestrian flow. The present work is motivated by the recent pedestrian experiments and modeling discussed in [2, 19], where the authors consider the pedestrian motion in a circle and model the crowd movement using a system of 1-D PDEs.

The major advantage of the CA formalism is that it allows for a systematic derivation of the coarse-grained dynamics. The main assumptions about the traffic flow (vehicular or pedestrian) are build into the microscopic model. The derivation of the coarse-grained description typically requires some simplifying assumptions about the statistical behavior of the microscopic model which can be numerically verified.

The main conceptual difference between the CA models of the vehicular traffic and the CA model studied in this paper is that the pedestrian motion is bi-directional which leads to completely new paradigms. In particular, the coarse-grained description of the pedestrian traffic becomes a system of conservation laws which is only conditionally hyperbolic. We demonstrate that this system may exhibit an unrealistic nonhyperbolic behavior, depending on the magnitude of the density of the pedestrian traffic. To overcome this difficulty, we systematically derive nonlinear diffusive corrections to the PDE model from the original microscopic description.

The paper is organized as follows. In Section 2, we introduce the microscopic CA model. In Sections 3 and 4, we discuss the derivation of the mesoscopic and macroscopic analogs for the density of the pedestrian traffic, as well as derive the next-order nonlinear diffusive corrections for the macroscopic PDE model. In Section 5, we describe several sets of simulations, in which the microscopic and macroscopic PDE models are compared illustrating, in particular, the effect of diffusion for the initial conditions leading to the regime of nonhyperbolicity of the inviscid macroscopic PDE model. Finally, in Appendix A, we provide a brief description of the numerical method used to solve the derived systems of PDEs.

2   Microscopic Pedestrian Model

To construct the microscopic model, we consider the time evolution of a 1-D lattice $\mathcal{L}$ with pedestrians moving into two opposite directions. The process is schematically illustrated in Figure 2.1.

The main difference with previous works on car traffic models (e.g. [21]) is that the pedestrians can move into opposite directions and we need to specify explicit rules when two such pedestrians meet. We represent pedestrians moving to the right and to the left by the variables $\sigma_k^+(t) \equiv \sigma^+(k, t)$
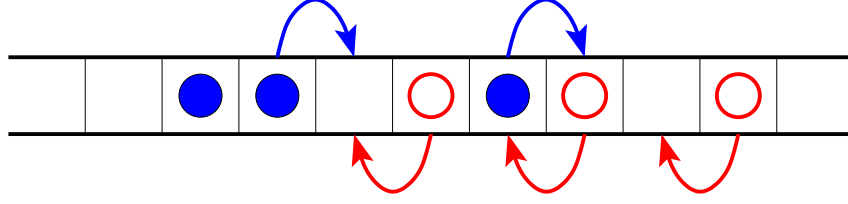
Figure 2.1: Schematic pedestrian configuration: Filled and empty circles represent pedestrians moving to the right and left, respectively. Arrows represent possible pedestrian movements in this configuration.

and $\sigma_k^-(t) \equiv \sigma^-(k, t)$, respectively, where k is the position on the lattice and t denotes time:

$$\sigma_k^\pm(t) = \begin{cases} 1, & \text{if at time } t \text{ cell } k \text{ is occupied by a pedestrian moving to the right (left),} \\ 0, & \text{otherwise.} \end{cases}$$

Moreover, we assume that pedestrians moving into two opposite directions can occupy the same cell (i.e., it is possible to have $\sigma_k^+(t) = \sigma_k^-(t) = 1$ for some k), but their velocities are reduced in that case. This mimics the slowdown due to side-stepping in more realistic CA models [5, 9] when pedestrians are avoiding the upcoming traffic. We also assume that pedestrians moving in the same direction cannot occupy the same cell. For simplicity of the presentation, we omit the notation for the time-dependence of σ_k^+ and σ_k^- for the rest of the paper.

To complete the construction of the microscopic CA model, we consider explicit rules for the slowdown interaction which describe how the velocity changes when pedestrians moving in opposite directions come in contact (i.e., occupy the same cell or two neighboring cells). In particular, we explicitly prescribe velocities for four different pedestrian configurations in the cells neighboring to the right-moving pedestrian with $\sigma_k^+ = 1$ (assuming that $\sigma_{k+1}^+ = 0$):

$$\begin{cases} c_0, & \text{if } \sigma_k^- = \sigma_{k+1}^- = 0 \text{ (no left-moving pedestrians in cells } k \text{ or } k+1), \\ c_1, & \text{if } \sigma_k^- = 1, \sigma_{k+1}^- = 0 \text{ (a left-moving pedestrian is in cell } k), \\ c_2, & \text{if } \sigma_k^- = 0, \sigma_{k+1}^- = 1 \text{ (a left-moving pedestrian is in cell } k+1), \\ c_3, & \text{if } \sigma_k^- = \sigma_{k+1}^- = 1 \text{ (left-moving pedestrians in cells } k \text{ and } k+1). \end{cases}$$

Notice that from the common sense considerations, the velocities should obey the following relationship: $c_3 < c_2 \approx c_1 < c_0$. The velocities of the left-moving pedestrian $\sigma_k^- = 1$ can be obtain in a similar manner.

The prescribed velocities are used to determine the probability of a pedestrian to move to the neighboring cell, that is, the probability of transition $k \to k+1$ for σ_k^+ during a small time interval Δt is

$$\begin{aligned} P_{k \to k+1}^+ = \Delta t \Big[& c_0 \sigma_k^+ (1 - \sigma_{k+1}^+)(1 - \sigma_k^-)(1 - \sigma_{k+1}^-) + c_1 \sigma_k^+ (1 - \sigma_{k+1}^+) \sigma_k^- (1 - \sigma_{k+1}^-) \\ & + c_2 \sigma_k^+ (1 - \sigma_{k+1}^+)(1 - \sigma_k^-) \sigma_{k+1}^- + c_3 \sigma_k^+ (1 - \sigma_{k+1}^+) \sigma_k^- \sigma_{k+1}^- \Big], \end{aligned} \tag{2.1}$$

while the probability of transition $k \to k-1$ for σ_k^- is

$$\begin{aligned} P_{k \to k-1}^- = \Delta t \Big[& c_0 \sigma_k^- (1 - \sigma_{k-1}^-)(1 - \sigma_{k-1}^+)(1 - \sigma_k^+) + c_1 \sigma_k^- (1 - \sigma_{k-1}^-)(1 - \sigma_{k-1}^+) \sigma_k^+ \\ & + c_2 \sigma_k^- (1 - \sigma_{k-1}^-) \sigma_{k-1}^+ (1 - \sigma_k^+) + c_3 \sigma_k^- (1 - \sigma_{k-1}^-) \sigma_{k-1}^+ \sigma_k^+ \Big]. \end{aligned} \tag{2.2}$$

The lattice configurations $\boldsymbol{\sigma}_t^- := \{\sigma_k^-\}$ and $\boldsymbol{\sigma}_t^+ := \{\sigma_k^+\}$ together constitute a continuous-time Markov chain for $\boldsymbol{\sigma}_t := \{\boldsymbol{\sigma}_t^-, \boldsymbol{\sigma}_t^+\}$. This model is easily simulated numerically using the Metropolis algorithm for computing the expected values of σ^- and σ^+. One can develop a Kinetic Monte-Carlo algorithm for these problems, but we found that the Metropolis algorithm was quite efficient when the velocities c_0, c_1, c_2, c_3 are not very small. We expect the Metropolis algorithm might become inefficient when these velocities are $\sim 10^{-2}$ and a Kinetic-Monte Carlo might be necessary to perform faster simulations of the stochastic system.

Since $\boldsymbol{\sigma}_t$ is a continuous-time stochastic process, its generator is defined by

$$A\psi = \lim_{\Delta t \to 0} \frac{\mathbb{E}\psi(\boldsymbol{\sigma}_{\Delta t}) - \psi(\boldsymbol{\sigma}_0)}{\Delta t},$$

where $\boldsymbol{\sigma}_0$ is the initial configuration, $\boldsymbol{\sigma}_{\Delta t}$ is the configuration at time Δt, ψ is any test function, and the expectation is taken over all possible transitions from $\boldsymbol{\sigma}_0$ to $\boldsymbol{\sigma}_{\Delta t}$. The generator of this stochastic process can be computed as follows:

$$A\psi = \frac{1}{\Delta t} \sum_k \left\{ P_{k\to k+1}^+ \left[\psi(\boldsymbol{\sigma}_{k\leftrightarrow k+1}^+, \boldsymbol{\sigma}_0^-) - \psi(\boldsymbol{\sigma}_0) \right] + P_{k\to k-1}^- \left[\psi(\boldsymbol{\sigma}_0^+, \boldsymbol{\sigma}_{k\leftrightarrow k-1}^-) - \psi(\boldsymbol{\sigma}_0) \right] \right\}, \quad (2.3)$$

where $\boldsymbol{\sigma}_{k\leftrightarrow k+1}^+$ is the configuration obtained from $\boldsymbol{\sigma}_0^+$ by exchanging the values in cells k and $k+1$, and similarly, $\boldsymbol{\sigma}_{k\leftrightarrow k-1}^-$ is the configuration obtained from $\boldsymbol{\sigma}_0^-$ by exchanging the values in cells k and $k-1$. To derive the coarse-grain model, we need to compute the generator (2.3) in two particular cases: For $\psi(\boldsymbol{\sigma}^+, \boldsymbol{\sigma}^-) = \sigma_k^+$ and $\psi(\boldsymbol{\sigma}^+, \boldsymbol{\sigma}^-) = \sigma_k^-$, we obtain

$$A\sigma_k^+ = \frac{P_{k-1\to k}^+ - P_{k\to k+1}^+}{\Delta t} \quad \text{and} \quad A\sigma_k^- = \frac{P_{k+1\to k}^- - P_{k\to k-1}^-}{\Delta t}, \quad (2.4)$$

respectively.

3 Mesoscopic Model

In this section, we use the microscopic CA model presented in Section 2 to derive the mesoscopic model for the densities $\rho_k^\pm := \mathbb{E}\sigma_k^\pm$ (once again, to simplify notation, the time-dependence of $\rho_k^\pm$ is omitted throughout the paper). To this end, we first recall that the generator A satisfies the following property:

$$\frac{d}{dt}\mathbb{E}\psi = \mathbb{E}A\psi,$$

which can be applied to the test functions $\psi = \sigma_k^+$ and $\psi = \sigma_k^-$. This together with (2.1), (2.2) and (2.4) results in the equations for the time-evolution of $\rho_k^\pm$:

$$
\begin{aligned}
\frac{d\rho_k^+}{dt} = \mathbb{E}\big[& c_0\sigma_{k-1}^+(1-\sigma_k^+)(1-\sigma_{k-1}^-)(1-\sigma_k^-) - c_0\sigma_k^+(1-\sigma_{k+1}^+)(1-\sigma_k^-)(1-\sigma_{k+1}^-) \\
& +c_1\sigma_{k-1}^+(1-\sigma_k^+)\sigma_{k-1}^-(1-\sigma_k^-) - c_1\sigma_k^+(1-\sigma_{k+1}^+)\sigma_k^-(1-\sigma_{k+1}^-) \\
& +c_2\sigma_{k-1}^+(1-\sigma_k^+)(1-\sigma_{k-1}^-)\sigma_k^- - c_2\sigma_k^+(1-\sigma_{k+1}^+)(1-\sigma_k^-)\sigma_{k+1}^- \\
& +c_3\sigma_{k-1}^+(1-\sigma_k^+)\sigma_{k-1}^-\sigma_k^- - c_3\sigma_k^+(1-\sigma_{k+1}^+)\sigma_k^-\sigma_{k+1}^- \big],
\end{aligned}
$$

$$
\begin{aligned}
\frac{d\rho_k^-}{dt} = \mathbb{E}\big[& c_0\sigma_{k+1}^-(1-\sigma_k^-)(1-\sigma_k^+)(1-\sigma_{k+1}^+) - c_0\sigma_k^-(1-\sigma_{k-1}^-)(1-\sigma_{k-1}^+)(1-\sigma_k^+) \\
& +c_1\sigma_{k+1}^-(1-\sigma_k^-)(1-\sigma_k^+)\sigma_{k+1}^+ - c_1\sigma_k^-(1-\sigma_{k-1}^-)(1-\sigma_{k-1}^+)\sigma_k^+ \\
& +c_2\sigma_{k+1}^-(1-\sigma_k^-)\sigma_k^+(1-\sigma_{k+1}^+) - c_2\sigma_k^-(1-\sigma_{k-1}^-)\sigma_{k-1}^+(1-\sigma_k^+) \\
& +c_3\sigma_{k+1}^-(1-\sigma_k^-)\sigma_k^+\sigma_{k+1}^+ - c_3\sigma_k^-(1-\sigma_{k-1}^-)\sigma_{k-1}^+\sigma_k^+ \big].
\end{aligned}
$$

(3.1)

The system (3.1) is exact, but not closed, since its right-hand side involves higher-order moments. The closure approximation can be derived by assuming that the joint measure for σ^+ and σ^- is approximately a product measure. This implies, for instance, that adjacent cells are approximately independent and, in particular, $\mathbb{E}[\sigma_k^\pm \sigma_{k+1}^\pm] \approx \mathbb{E}\sigma_k^\pm \mathbb{E}\sigma_{k+1}^\pm$. Thus, a closed system of equations for $\rho_k^\pm$ can be obtained and the resulting mesoscopic model for the pedestrian density reads

$$
\begin{aligned}
\frac{d\rho_k^+}{dt} =& c_0\rho_{k-1}^+(1-\rho_k^+)(1-\rho_{k-1}^-)(1-\rho_k^-) - c_0\rho_k^+(1-\rho_{k+1}^+)(1-\rho_k^-)(1-\rho_{k+1}^-) \\
& +c_1\rho_{k-1}^+(1-\rho_k^+)\rho_{k-1}^-(1-\rho_k^-) - c_1\rho_k^+(1-\rho_{k+1}^+)\rho_k^-(1-\rho_{k+1}^-) \\
& +c_2\rho_{k-1}^+(1-\rho_k^+)(1-\rho_{k-1}^-)\rho_k^- - c_2\rho_k^+(1-\rho_{k+1}^+)(1-\rho_k^-)\rho_{k+1}^- \\
& +c_3\rho_{k-1}^+(1-\rho_k^+)\rho_{k-1}^-\rho_k^- - c_3\rho_k^+(1-\rho_{k+1}^+)\rho_k^-\rho_{k+1}^-,
\end{aligned}
$$

$$
\begin{aligned}
\frac{d\rho_k^-}{dt} =& c_0\rho_{k+1}^-(1-\rho_k^-)(1-\rho_k^+)(1-\rho_{k+1}^+) - c_0\rho_k^-(1-\rho_{k-1}^-)(1-\rho_{k-1}^+)(1-\rho_k^+) \\
& +c_1\rho_{k+1}^-(1-\rho_k^-)(1-\rho_k^+)\rho_{k+1}^+ - c_1\rho_k^-(1-\rho_{k-1}^-)(1-\rho_{k-1}^+)\rho_k^+ \\
& +c_2\rho_{k+1}^-(1-\rho_k^-)\rho_k^+(1-\rho_{k+1}^+) - c_2\rho_k^-(1-\rho_{k-1}^-)\rho_{k-1}^+(1-\rho_k^+) \\
& +c_3\rho_{k+1}^-(1-\rho_k^-)\rho_k^+\rho_{k+1}^+ - c_3\rho_k^-(1-\rho_{k-1}^-)\rho_{k-1}^+\rho_k^+.
\end{aligned}
$$

(3.2)

Note that the system (3.2) is defined on the same lattice $\mathcal{L}$ as the microscopic model.

4   Macroscopic PDE Model

We now treat sites $k \in \mathcal{L}$ as cells with some fixed length $h > 0$. Let Ω denote a subdomain of $\mathbb{R}$ corresponding to the lattice $\mathcal{L}$, i.e., $\Omega = [0, L]$ (the number of cells, of course, depends on h). We consider a rescaling of time $t \to ht$ and derive a coarse-grained PDE model in the limit as the cell size tends to zero and the number of cells tends to infinity.

To this end, we rewrite the system (3.2) in the following flux form (taking the time rescaling into account):

$$
\frac{d\rho_k^+}{dt} = -\frac{F_{k,k+1}^+ - F_{k-1,k}^+}{h}, \qquad \frac{d\rho_k^-}{dt} = \frac{F_{k,k+1}^- - F_{k-1,k}^-}{h},
$$

(4.1)

where

$$F_{k,k+1}^+ = \rho_k^+(1 - \rho_{k+1}^+)\left[(1 - \rho_{k+1}^-)\left(c_0(1 - \rho_k^-) + c_1\rho_k^-\right) + \rho_{k+1}^-\left(c_2(1 - \rho_k^-) + c_3\rho_k^-\right)\right],$$
$$F_{k,k+1}^- = \rho_{k+1}^-(1 - \rho_k^-)\left[(1 - \rho_k^+)\left(c_0(1 - \rho_{k+1}^+) + c_1\rho_{k+1}^+\right) + \rho_k^+\left(c_2(1 - \rho_{k+1}^+) + c_3\rho_{k+1}^+\right)\right]. \tag{4.2}$$

Multiplying the above equations by $\varphi_k := \varphi(kh)$, where $\varphi \in C_0^1(\overline{\Omega})$ is a test function, and using the summation by parts property over Ω, yields

$$\sum_k \varphi_k \frac{d\rho_k^\pm}{dt} = \pm \sum_k F_{k,k+1}^\pm \frac{\varphi_{k+1} - \varphi_k}{h}. \tag{4.3}$$

Next, we multiply equation (4.3) by h and expand φ_{k+1} in a Taylor series about kh to obtain

$$\sum_k \varphi_k \frac{d\rho_k^\pm}{dt} h = \pm \sum_k F_{k,k+1}^\pm [\varphi_k' + \mathcal{O}(h)]h. \tag{4.4}$$

We define pedestrian densities on Ω as follows. Again, using the notation $\rho^\pm$ (for convenience), define the function $\rho^\pm(x,t)$ as a continuous piecewise linear interpolation (in the spatial variable) of $\rho_k^\pm(t)$ and take the limit as $h \to 0^+$. Due to the boundeness of both $\rho^\pm$ and $\frac{d\rho_k^\pm}{dt}$ we obtain a weak formulation of the coarse-grained model:

$$\int_\Omega \varphi(x) \frac{\partial}{\partial t} \rho^\pm(x,t)\, dx = \pm \int_\Omega F^\pm(\rho^+, \rho^-)\varphi'(x)\, dx, \tag{4.5}$$

where $F^\pm(\rho^+, \rho^-)$ are defined as the corresponding limits of $F_{k,k+1}^\pm$, i.e.,

$$F^+(\rho^+, \rho^-) = f(\rho^+)g(\rho^-), \quad F^-(\rho^+, \rho^-) = f(\rho^-)g(\rho^+),$$

where
$$f(u) = u(1 - u), \quad g(u) = (c_3 - c_2 - c_1 + c_0)u^2 + (c_2 + c_1 - 2c_0)u + c_0. \tag{4.6}$$

Since φ is arbitrary, the integral equations (4.5) can be written as the following system of PDEs:

$$\frac{\partial \rho^+}{\partial t} + \frac{\partial}{\partial x}\left[f(\rho^+)g(\rho^-)\right] = 0, \quad \frac{\partial \rho^-}{\partial t} - \frac{\partial}{\partial x}\left[f(\rho^-)g(\rho^+)\right] = 0. \tag{4.7}$$

Remark 4.1 Note that the velocities c_1 and c_2 enter only as a sum into (4.6). Therefore, it is not necessary to specify them separately.

Remark 4.2 The coarse-grained system (4.7) is only conditionally hyperbolic. Indeed, the Jacobian

$$\begin{pmatrix} f'(\rho^+)g(\rho^-) & f(\rho^+)g'(\rho^-) \\ -f(\rho^-)g'(\rho^+) & -f'(\rho^-)g(\rho^+) \end{pmatrix} \tag{4.8}$$

has real eigenvalues only if

$$\left[f'(\rho^-)g(\rho^+) + f'(\rho^+)g(\rho^-)\right]^2 - 4f(\rho^-)f(\rho^+)g'(\rho^-)g'(\rho^+) > 0. \tag{4.9}$$

Therefore, for any particular choice of velocities c_0, c_1, c_2, and c_3 there is a region on nonhyperbolicity in the (ρ^-, ρ^+) plane. From (4.6), one can see that the nonhyperbolicty can only manifest itself when pedestrians moving in two opposite directions are both present in a particular location. Two examples of nonhyperbolic regions are plotted in Figure 4.1. The nonhyperbolic region described in (4.9) depends only on the ratio of velocities c_1/c_0, c_2/c_0, and c_3/c_0, but not on the particular value of c_0. The region of nonhyperbolicity becomes larger as the slowdown effect becomes more pronounces (i.e., as the ratios c_1/c_0, c_2/c_0, and c_3/c_0 become smaller). The loss of hyperbolicity may induce instabilities (as illustrated in Section 5), which are nonphysical and can be removed by introducing a nonlinear diffusive correction to the system (as we demonstrate in the next section).
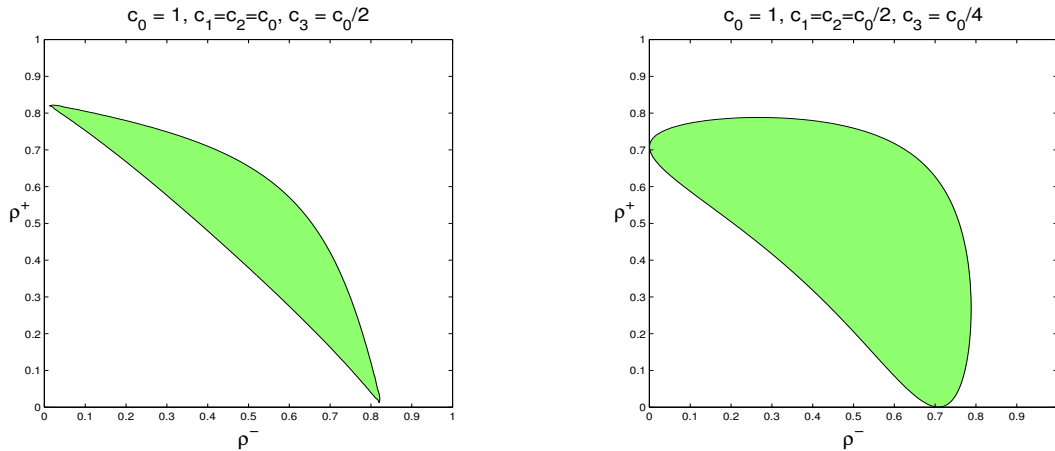

Figure 4.1: Regions of nonhyperbolicity (inside) in the ρ^+, ρ^- plane for the equation (4.7) for two particular choices of velocities: $c_0 = 1$, $c_1 = c_2 = c_0$, $c_3 = c_0/2$ (left) and $c_0 = 1$, $c_1 = c_2 = c_0/2$, $c_3 = c_0/4$ (right).

Remark 4.3 The flux function $F^+(\rho^+, \rho^-) = f(\rho^+)g(\rho^-)$ for two different choices of velocities is depicted in Figure 4.2. For the unidirectional flow, the coarse-grained model (4.7) is equivalent to the Lighthill-Whitham-Richards model of car traffic with the symmetric flux of the form $\rho(1-\rho)$. Moreover, the flux $F^+(\rho^+, \rho^-)$ is always symmetric about the plane $\rho^+ = 1/2$ due to the particular structures of F^+.

In Figure 4.3, we plot the total flux defined as $F^+ + F^-$ for two particular relationships between ρ^+ and ρ^-. This demonstrates that the total flux can become non-symmetric for the bidirectional flow with the heavier right tail. This is consistent with the experimental results reported in [23,24].

The stochastic CA model described in this paper can be generalized to include the look-ahead potential and the corresponding coarse-grained PDE with look-ahead terms can be derived similarly to [7,21]. We expect that a more general form of the flux (including highly non-symmetric) can be obtained by including the look-ahead potential into the model. However, strong look-ahead potentials are likely to destroy the approximate independence assumption [12] and a more empirical closure might be necessary. Nevertheless, the one-sided interactions induced by the look-ahead potential would result in a highly non-symmetric flux functions and more general fundamental diagrams. This work will be carried out in a subsequent paper.
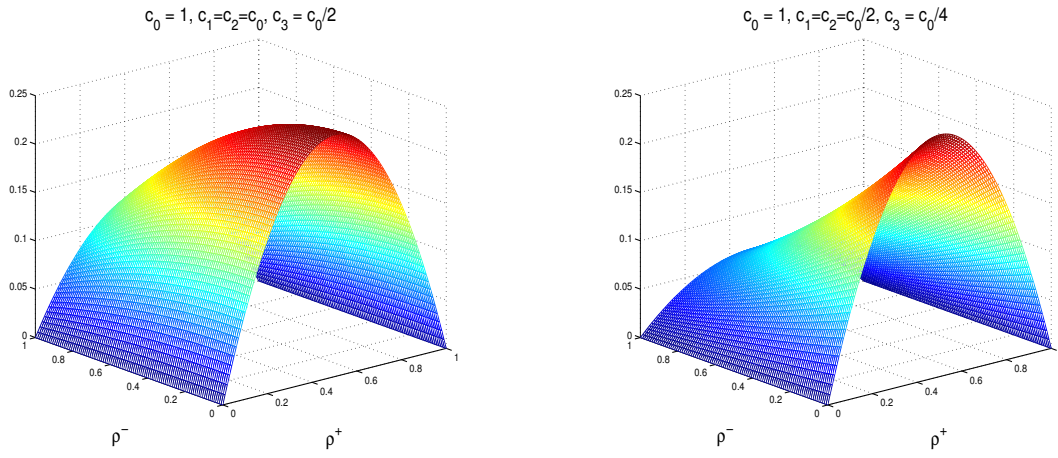
Figure 4.2: Flux function $F^+(\rho^+, \rho^-) = f(\rho^+)g(\rho^-)$ with f and g in (4.6) for two particular choices of velocities: $c_0 = 1$, $c_1 = c_2 = c_0$, $c_3 = c_0/2$ (left) and $c_0 = 1$, $c_1 = c_2 = c_0/2$, $c_3 = c_0/4$ (right).
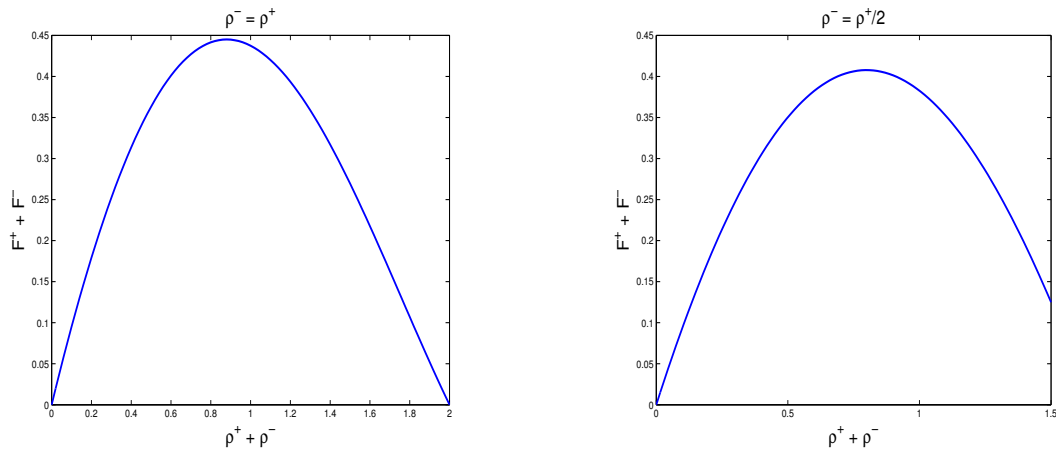

Figure 4.3: Total Flux $F^+(\rho^+, \rho^-) + F^-(\rho^+, \rho^-)$ for the velocities $c_0 = 1$, $c_1 = c_2 = c_0$, $c_3 = c_0/2$ and two particular relationships between ρ^+ and ρ^-: $\rho^- = \rho^+$ (left) and $\rho^- = \rho^+/2$ (right).

4.1 Diffusive Correction

The derivation of the coarse-grained PDE system (4.7), (4.6) can also be obtained by formally using the Taylor expansions

$$\rho_{k\pm1}^{\pm} = \rho_k^{\pm} \pm h(\rho_k^{\pm})' + \frac{h^2}{2}(\rho_k^{\pm})'' + \mathcal{O}(h^3)$$

in the flux formulation (4.1), (4.2) followed by passing to the limit as $h \to 0^+$.

Alternatively, keeping h fixed and neglecting the $\mathcal{O}(h^3)$ terms, leads to the following second-order PDE system, which contains nonlinear diffusion terms:

$$\frac{\partial \rho^+}{\partial t} + \frac{\partial}{\partial x}\left[f(\rho^+)g(\rho^-)\right] = h\Big[\frac{c_0}{2}\rho_{xx}^+ + \left(c_1 - c_0 + (c_3 - c_2 - c_1 + c_0)\rho^- + (c_2 - c_1)\rho^+\right)\rho_x^-\rho_x^+ +$$
$$\frac{1}{2}(c_1 - c_2)\rho^+(1 - \rho^+)\rho_{xx}^- + \frac{1}{2}\left((c_1 + c_2 - 2c_0)\rho^- + (c_3 - c_2 - c_1 + c_0)(\rho^-)^2\right)\rho_{xx}^+\Big],$$

$$\frac{\partial \rho^-}{\partial t} - \frac{\partial}{\partial x}\left[f(\rho^-)g(\rho^+)\right] = h\Big[\frac{c_0}{2}\rho_{xx}^- + \left(c_1 - c_0 + (c_3 - c_3 - c_1 + c_0)\rho^+ + (c_2 - c_1)\rho^-\right)\rho_x^+\rho_x^- +$$
$$\frac{1}{2}(c_1 - c_2)\rho^-(1 - \rho^-)\rho_{xx}^+ + \frac{1}{2}\left((c_2 + c_1 - 2c_0)\rho^+ + (c_3 - c_2 - c_1 + c_0)(\rho^+)^2\right)\rho_{xx}^-\Big].$$

The diffusion in the above system can be simplified considerably. Using the expressions for f and g in (4.6) we can rewrite the above system as

$$\frac{\partial \rho^+}{\partial t} + \frac{\partial}{\partial x}\left[f(\rho^+)g(\rho^-)\right] = \frac{\varepsilon}{2}\left[g(\rho^-)\rho_x^+ + (c_1 - c_2)f(\rho^+)\rho_x^-\right]_x,$$

$$\frac{\partial \rho^-}{\partial t} - \frac{\partial}{\partial x}\left[f(\rho^-)g(\rho^+)\right] = \frac{\varepsilon}{2}\left[g(\rho^+)\rho_x^- + (c_1 - c_2)f(\rho^-)\rho_x^+\right]_x. \tag{4.10}$$

Remark 4.4 It is easy to see that the coefficients of nonlinear diffusion are positive provided $c_1 \geq c_2$ and both ρ^+ and ρ^- are between 0 and 1. In the present work, we make an additional simplifying assumption $c_1 = c_2$ which considerably simplifies the diffusion terms. This is motivated by the fact that the velocities c_1 and c_2 only enter as a sum into the fluxes (see Remark 4.1) and both velocities correspond to a slowdown due to the presence of one pedestrian moving in the opposite direction. Therefore, we expect that the slowdown effect is equal in the limiting case of small cells.

Remark 4.5 The nonlinear diffusion in (4.10) reflects the presence of pedestrians moving in the opposite direction. For instance, the diffusion coefficient in the first, ρ^+-equation depends on ρ^-. It is instructive to consider the limiting cases: If $\rho^- = 0$ (i.e., no pedestrians moving to the left are present), the diffusion reduces to the usual linear diffusion $0.5\varepsilon c_0\rho_{xx}^+$, while if $\rho^- = 1$, then the diffusion becomes $0.5\varepsilon c_3\rho_{xx}^+$. The latter is, again, a linear diffusion, but with a smaller coefficient (since $c_3 < c_0$) reflecting a high density presence of the pedestrians moving in the opposite direction. Particular shape of the nonlinear diffusion coefficient is depicted in Figure 4.4 for two different choices of velocities.

Remark 4.6 It should be observed that the stochastic CA model is more diffusive in nature than the corresponding coarse-grained PDE system. This is a direct consequence of the approximate independence assumption $\mathbb{E}[\sigma_k^{\pm}\sigma_{k+1}^{\pm}] \approx \mathbb{E}\sigma_k^{\pm}\mathbb{E}\sigma_{k+1}^{\pm}$ used in the derivation of the PDE model (4.7).
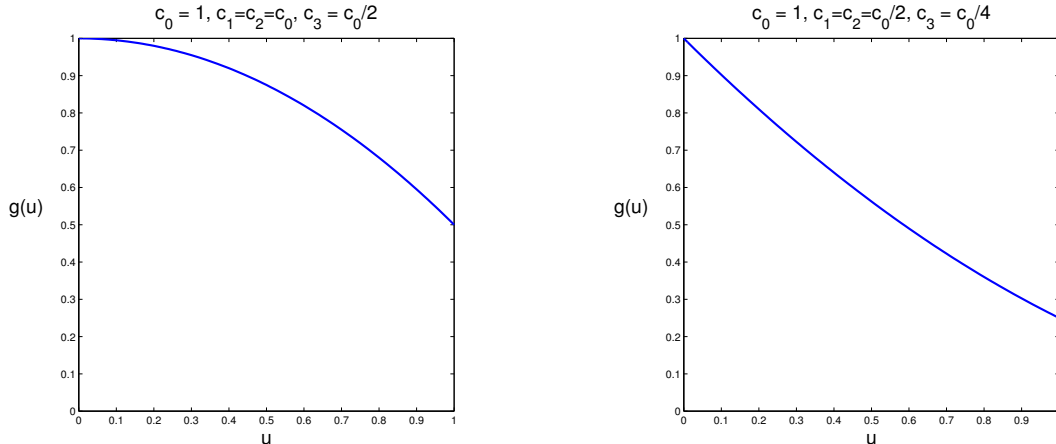
Figure 4.4: Nonlinear diffusion coefficient $g(u)$ as a function of u for two particular choices of velocities: $c_0 = 1$, $c_1 = c_2 = c_0$, $c_3 = c_0/2$ (left) and $c_0 = 1$, $c_1 = c_2 = c_0/2$, $c_3 = c_0/4$ (right).

It can be shown numerically that this assumption is valid only approximately which is manifested in a slightly wider spread of the ensemble in stochastic simulations than in the simulation of (4.7). Effectively, there are two sources of diffusion in the PDE model (4.7): (i) due to the finite cell size in stochastic simulations and (ii) due to small discrepancies in the approximate independence. Therefore, the value of ε has to be chosen empirically to match the stochastic simulations best.

5 Simulations

In this section, we present several sets of numerical experiments comparing and contrasting the propagation of pedestrian density in ensemble simulations of the microscopic stochastic model and the corresponding numerical solutions of the macroscopic PDE models (with and without diffusion). The mesoscopic model (3.2) can be considered as a conservative first-order finite-difference discretization of the PDE models and the results of the mesoscopic simulations (not shown in the paper), performed on a sufficiently fine grid, typically agree very well with the PDE results.

In all of the PDE simulations below, we implement a semi-discrete second-order central-upwind scheme from [16, 17] with the minmod parameter $\theta = 1$, CFL number equal to 0.5. The scheme is briefly described in Appendix A. It should be observed that the PDE simulations are performed on a much coarser mesh than the corresponding microscopic ones. We use periodic boundary conditions in all of the presented numerical examples.

In the first set of numerical experiments (Section 5.1), the initial conditions resemble the "red light" situation when a group of tightly packed pedestrians with density 1 is released at time $t = 0$. In the second set (Section 5.2), we mimic the pedestrian movements starting with fully mixed initial conditions sampled from a particular piecewise constant density. Finally, in Section 5.3, we illustrate the stabilizing effect of the diffusive corrections in the nonhyperbolic regime.

5.1 "Red Light" Initial Conditions

We first consider the microscopic CA model with the following initial conditions:

$$\sigma^+(k,0) = \begin{cases} 1, & n_1 \leq k \leq n_2, \\ 0, & \text{otherwise}, \end{cases} \qquad \sigma^-(k,0) = \begin{cases} 1, & N - n_2 \leq k \leq N - n_1, \\ 0, & \text{otherwise}, \end{cases} \tag{5.1}$$

with $n_2 - n_1 \ll N$. These initial conditions correspond to two (relatively small) groups of pedestrians standing still and starting to move toward each other at time $t = 0$. The velocities are taken as

$$c_0 = 0.8 m/s, \ c_1 = c_2 = c_0/a, \ c_3 = c_0/(2a), \tag{5.2}$$

where the parameter a describes the strength of the slowdown interactions, for which we consider two regimes with either $a = 2$ or $a = 3$. The parameters in the CA model are chosen so that the two groups are away from the boundary and, thus, boundary conditions do not affect the interaction:

$$N = 1400, \ n_1 = 301, \ n_2 = 340, \ h = 0.2 m, \ \Delta t = 0.01 s, \ MC = 5000, \tag{5.3}$$

where MC is the number of Monte-Carlo simulations.

The macroscopic simulations of the purely convective PDE system (4.7) are performed on the computational domain $[0, 280]$ with the mesh size $\Delta x = 0.8$ and initial data corresponding to (5.1):

$$\rho^+(x,0) = \begin{cases} 1, & 60 < x < 68, \\ 0, & \text{otherwise}, \end{cases} \qquad \rho^-(x,0) = \begin{cases} 1, & 212 < x < 220, \\ 0, & \text{otherwise}, \end{cases} \tag{5.4}$$

with the velocities c_0, c_1, c_2 and c_3 same as in (5.2).

The initial settings (5.1)–(5.3) and (5.4) correspond to the right- and left-moving groups, which initially do not overlap and their dynamics is equivalent to moving cars. After some time, the two groups begin to interact and we study how well the macroscopic PDE model reproduces these interactions. Figures 5.1 and 5.2 show comparison of the density profiles in CA and PDE simulations.

The macroscopic PDE model (4.7) produces very good results in the $a = 2$ regime. In particular, it reproduces the forward front at times $t = 80, 110$ and 140 quite well. The macroscopic results are slightly different from the stochastic ones after the two groups pass through each other (see times $t = 170$ and 210): The back front of moving pedestrians in simulations of the macroscopic model is sharper compared with the simulations of the stochastic model at these times. This can be explained by the purely hyperbolic nature of the macroscopic PDE for this range of the density values.

The $a = 3$ regime corresponds to stronger slowdown interactions between the two groups of pedestrians. We observe a considerable discrepancy between the CA and PDE models at times $t = 140, 170$ and 210. In particular, an effect similar to blocking occurs in the Monte-Carlo simulations of the stochastic model; this is especially evident at time $t = 170$. The propagation of two blocked groups resembles a slow diffusion over a barrier, whereas the simulations of the PDE model exhibit a faster propagating wave. Therefore, the PDE model with $a = 3$ seems to be outside of the range of validity of the closure approximations used in its derivation.

We note that the results obtained using the viscous PDE model (4.10) are quite similar to the inviscid ones: The diffusion simply smears the fronts but no substantially different phenomena have been observed.
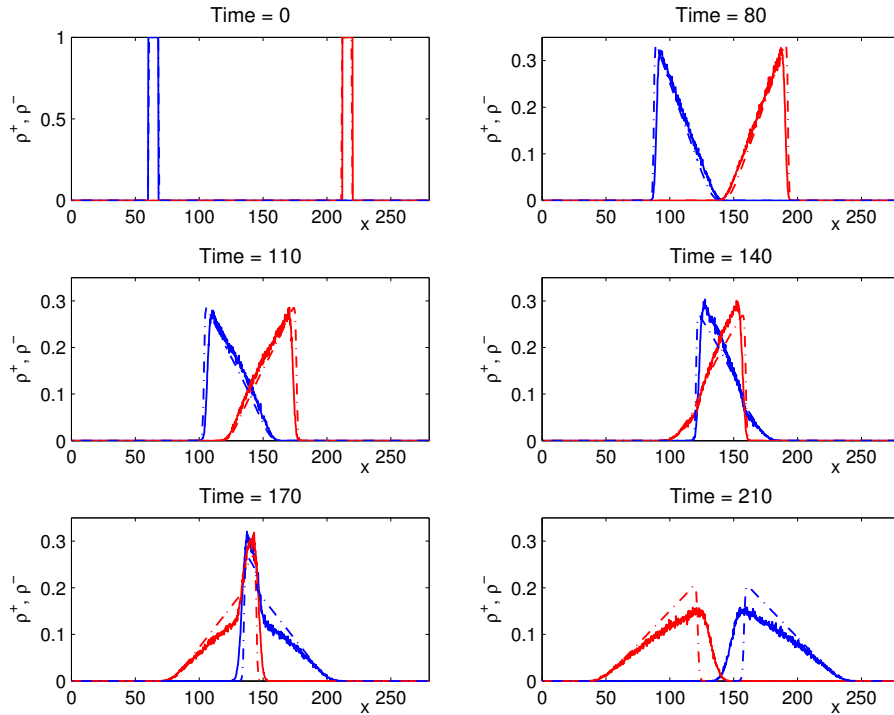
Figure 5.1: Comparison of the density profiles computed by the CA (solid line) and PDE (dash-dotted line) models with $a = 2$ and the "red light" initial conditions in (5.1) and (5.4). The right- (ρ^+) and left-moving (ρ^-) pedestrians are represented by the blue and red colors, respectively.
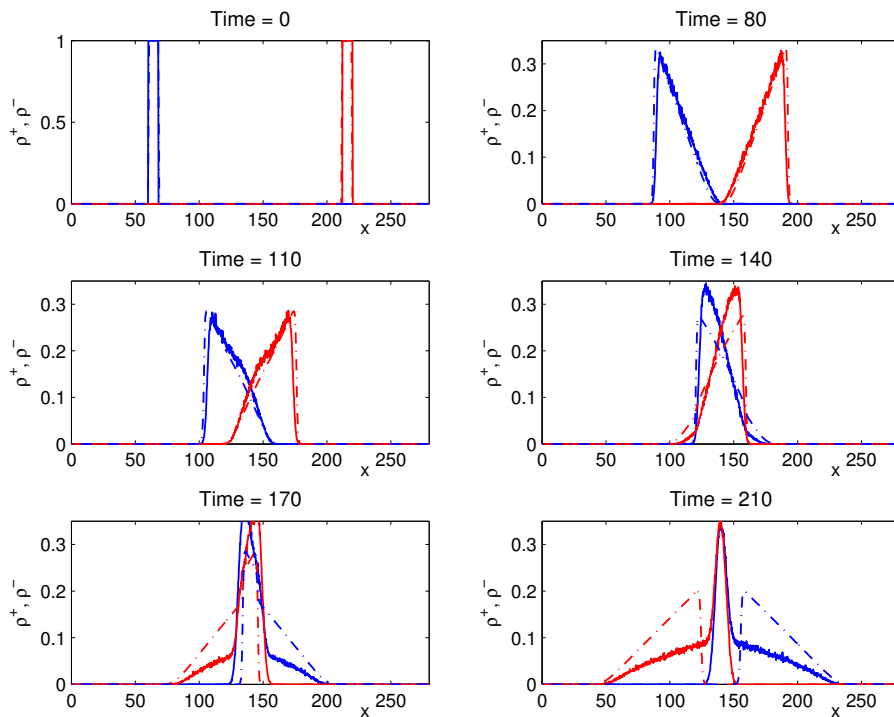

Figure 5.2: The same as in Figure 5.1 but with $a = 3$.

5.2   Fully Mixed Initial Conditions

In the second set of numerical experiments, we simulate pedestrian movement in a periodic domain, which is divided into 30 sectors with 15 cells in each sector (totally $N = 450$ cells). We initialize the CA simulations with the total number of 70 pedestrians (with 35 pedestrians moving in each direction). The initial numbers of right- and left-moving pedestrians in each sector are specified, while their distribution inside each sector is purely random (uniform). In dimensional units, each cell is $0.466m$ long, each sector is $7m$ long, and the domain is $210m$ long. Other parameters in the CA simulations are chosen to be $\Delta t = 0.005$ and $MC = 3000$.

The corresponding initial densities for the PDE models (4.7) and (4.10) are

$$\rho^{\pm}(x, 0) = \frac{n_i^{\pm}}{15} \quad \text{for} \quad \frac{i-1}{30}L < x < \frac{i}{30}L, \quad i = 1, \ldots, 30, \tag{5.5}$$

where n_i^+ and n_i^- are numbers of right- and left-moving pedestrians in the ith sector, respectively. The size of the computational domain is $L = 210$ and $\Delta x = 0.25$. In the simulations of the viscous PDE (4.10), we take the diffusion coefficient $\varepsilon = 0.5$.

As in Section 5.1, we take the velocities

$$c_0 = 1m/s, \quad c_1 = c_2 = c_0/a, \quad c_3 = c_0/(2a), \tag{5.6}$$

and perform two sets of numerical simulations with velocities with $a = 2$ and $a = 3$.

The obtained results are plotted in Figures 5.3–5.10. In the $a = 2$ case, the CA and PDE results are in a very good agreement, especially when the diffusion terms are included into the PDE models (Figures 5.3–5.6). By comparing Figures 5.3 and 5.5, one can see that the invscid PDE model preserves sharp boundaries between pedestrian clusters considerably longer than the CA or viscous PDE ones. The viscous PDE model reproduces the results of the stochastic simulations quite accurately, including the "stop-and-go" phenomenon observed there. The "stop-and-go" wave is most evident for the right-moving cluster of pedestrians at $\rho^+(x \approx 180, t = 0)$ (Figures 5.3 and 5.7). These results verify that the stochastic simulations are more diffusive due to the approximate independence assumption used in the derivation of the effective PDE model. Therefore, diffusive corrections are essential for reproducing the behavior of the stochastic model for longer times. When the slowdown interaction is stronger ($a = 3$), the difference between the CA and the inviscid PDE simulations are more pronounced: The stochastic "blocking" is more severe, while the PDE models develop both "blocking" and "stop-and-go" waves (see Figures 5.7–5.10).

Numerical solutions of the inviscid PDE model are expected to be influenced by a numerical diffusion especially when a coarse grid is used. To check the effect of the numerical diffusion, we perform a mesh refinement study. The results are presented in Figure 5.11, where we plot the snapshots of the PDE solution at a particular time $t = 25$ computed with different spatial resolutions. As one can see, the inviscid PDE solution is considerably affected by the size of the spatial discretization for lower resolutions. On the other hand, solutions of the viscous PDE are not visibly affected by the spatial discretization due to the presence of viscous terms. Grid refinement study has been performed for all simulations discussed in this paper, but it is not presented only for the brevity of the presentation.

5.3   Nonhyperbolic Regime

In both simulations described in Sections 5.1 and 5.2, the magnitude of pedestrian densities ρ^+ and ρ^- remain smaller than the critical values for the nonhyperbolic behavior (recall that the
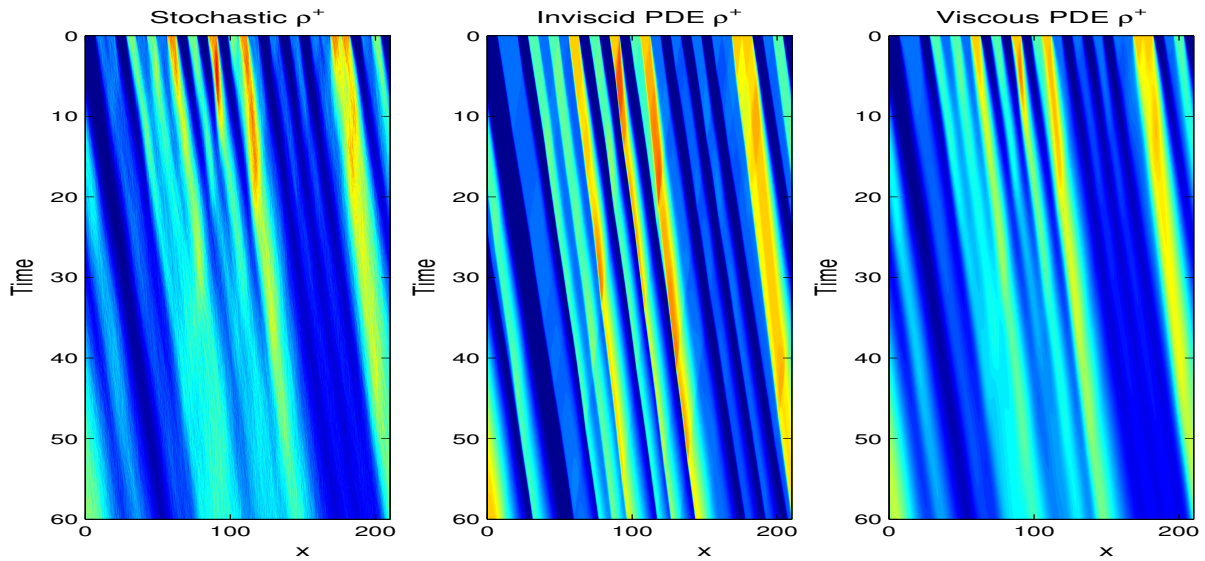
Figure 5.3: Dynamics of right-moving pedestrians in both the CA and PDE models with the fully mixed initial conditions (5.5) and velocities (5.6) with $a = 2$.
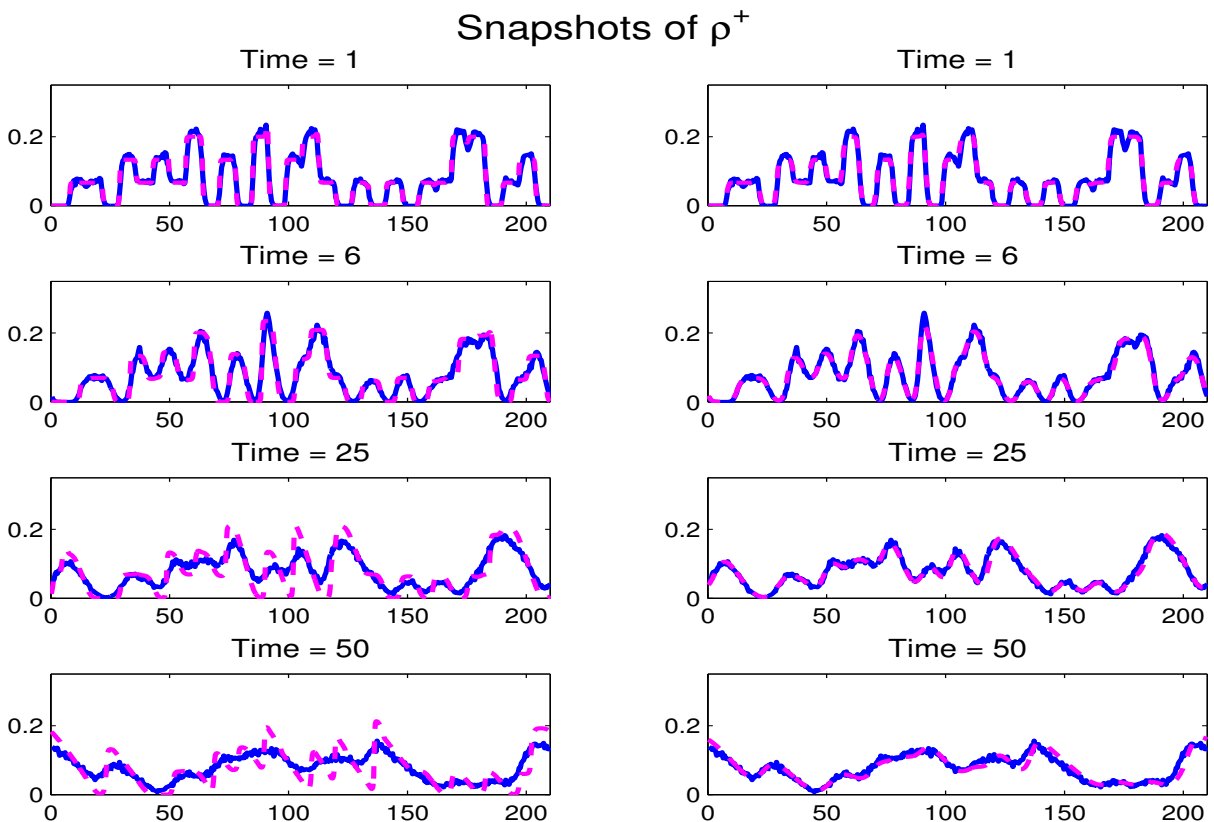

Figure 5.4: Time snapshots of the solutions from Figure 5.3. The solid blue line represents the CA solution, while the dashed magenta line represents the inviscid (left) and viscous with $\varepsilon = 0.5$ (right) PDE solutions.
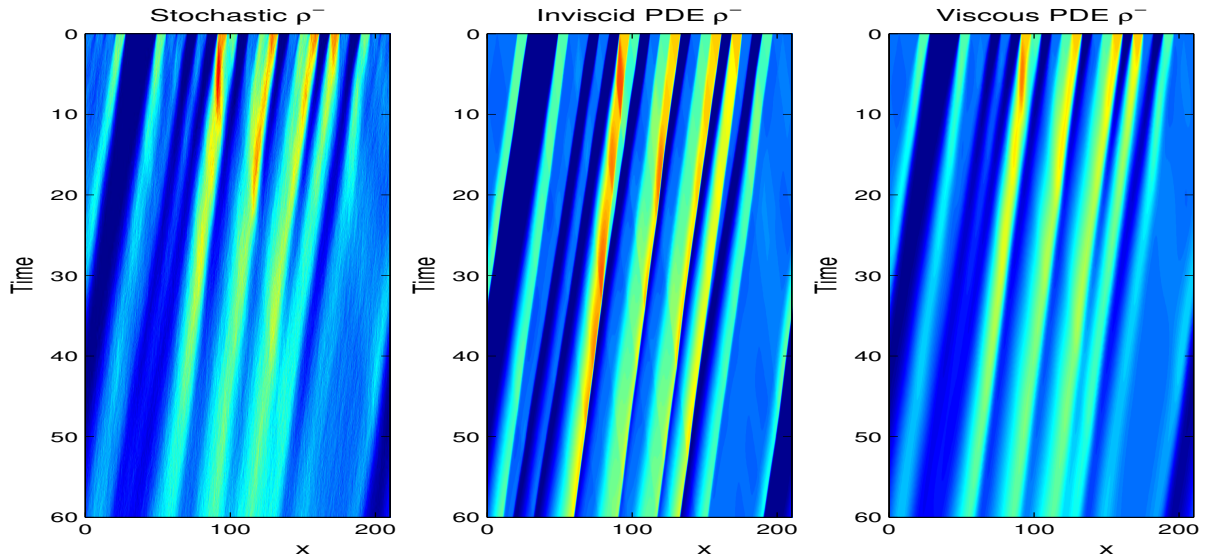
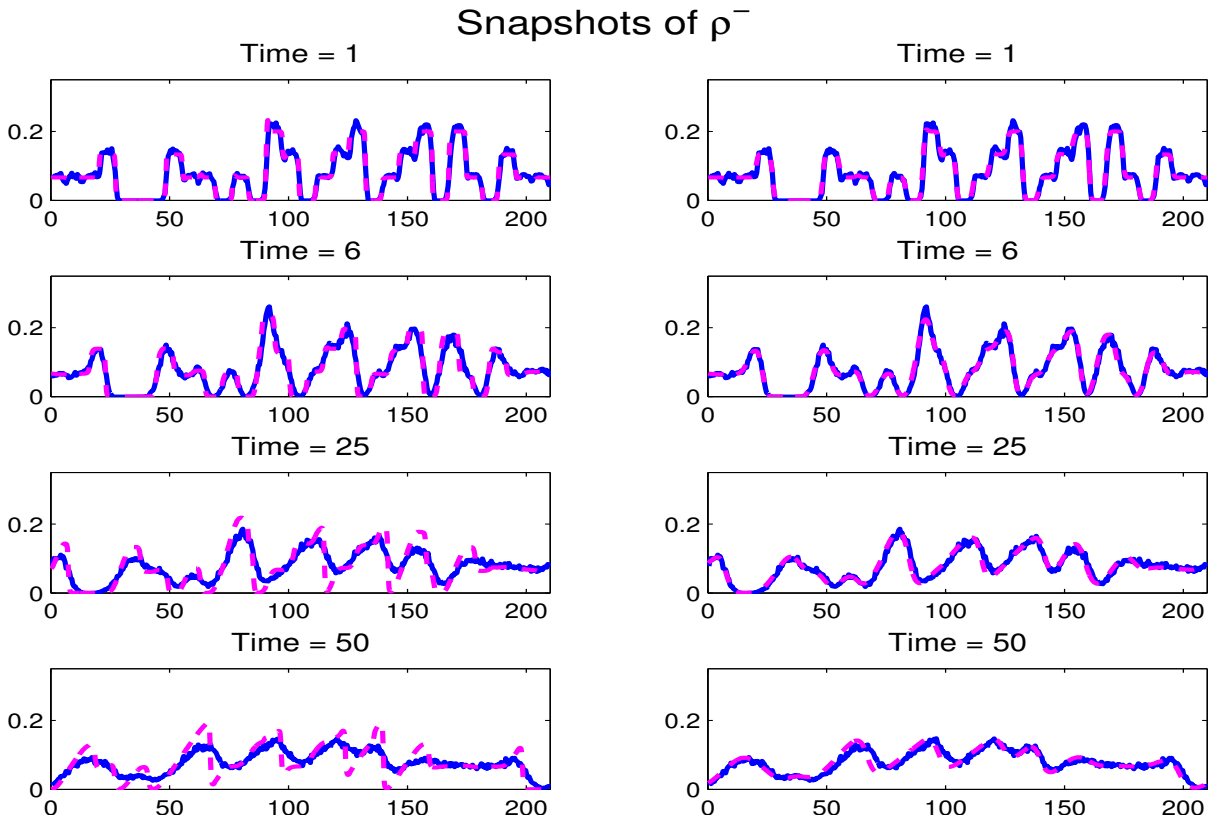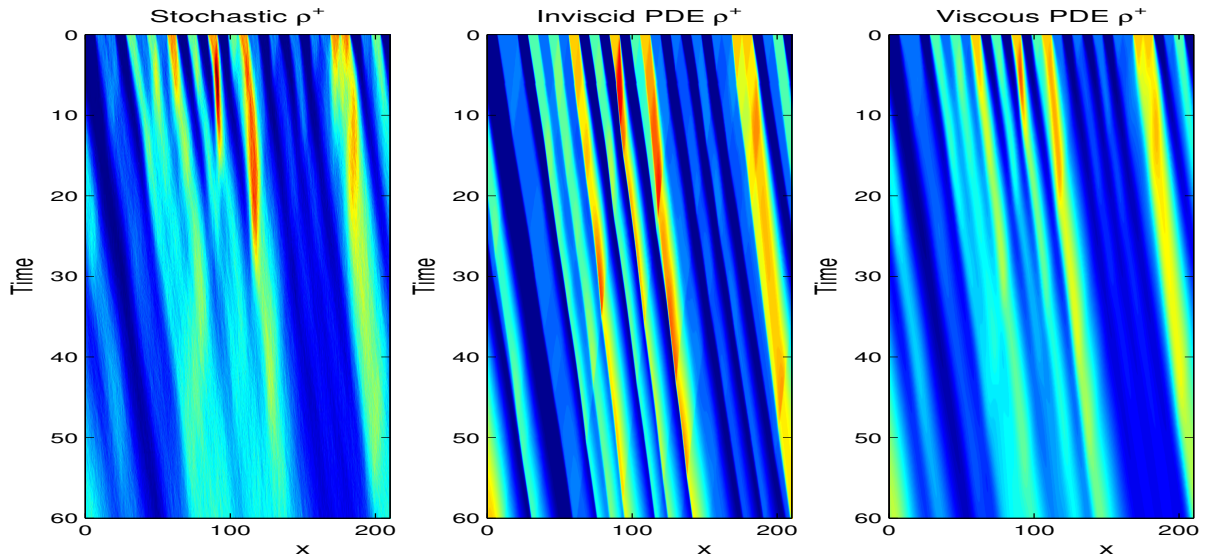Figure 5.5: The same as in Figure 5.3 but for left-moving pedestrians.

Snapshots of ρ^-

Figure 5.6: Time snapshots of the solution from Figure 5.5. The solid blue line represents the CA solution, while the dashed magenta line represents the inviscid (left) and viscous with $\varepsilon = 0.5$ (right) PDE solutions.

Figure 5.7: Dynamics of right-moving pedestrians in both the CA and PDE models with the fully mixed initial conditions (5.5) and velocities (5.6) with $a = 3$.
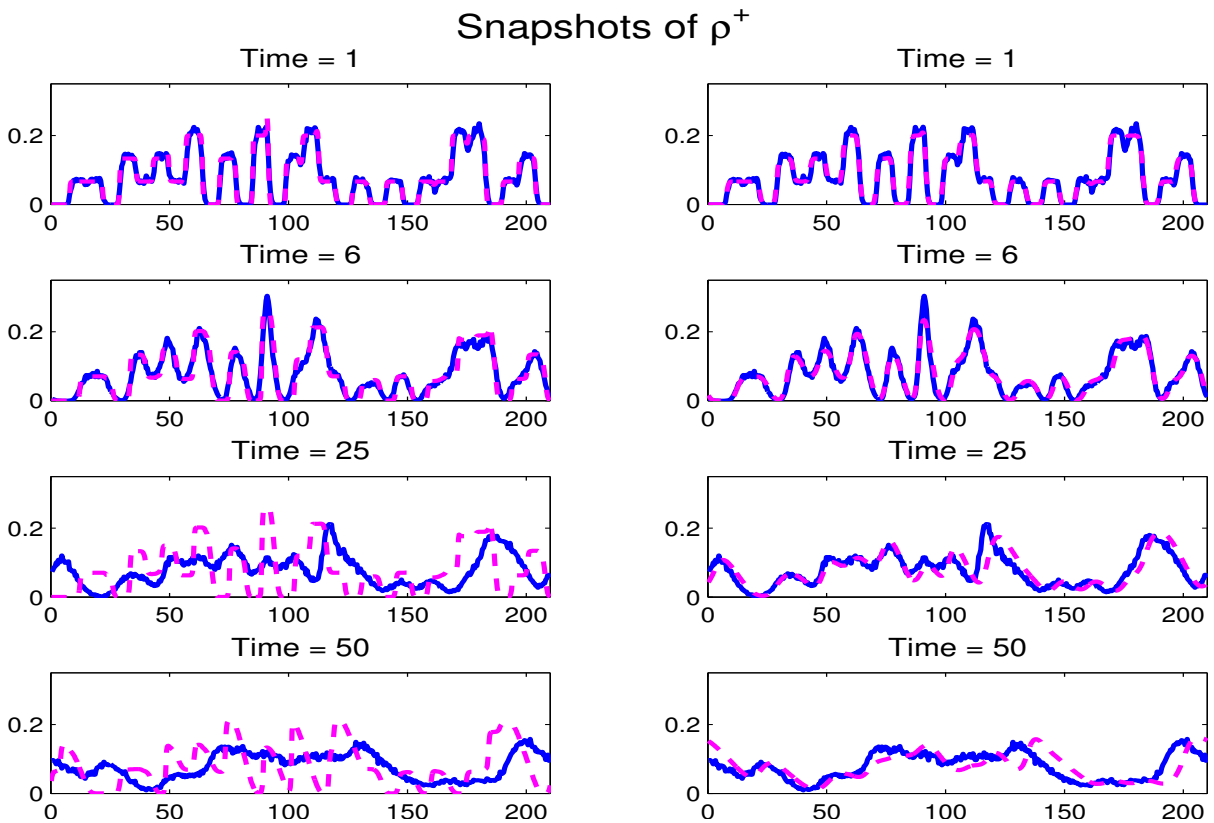

Figure 5.8: Time snapshots of the solutions from Figure 5.7. The solid blue line represents the CA solution, while the dashed magenta line represents the inviscid (left) and viscous with $\varepsilon = 0.5$ (right) PDE solutions.
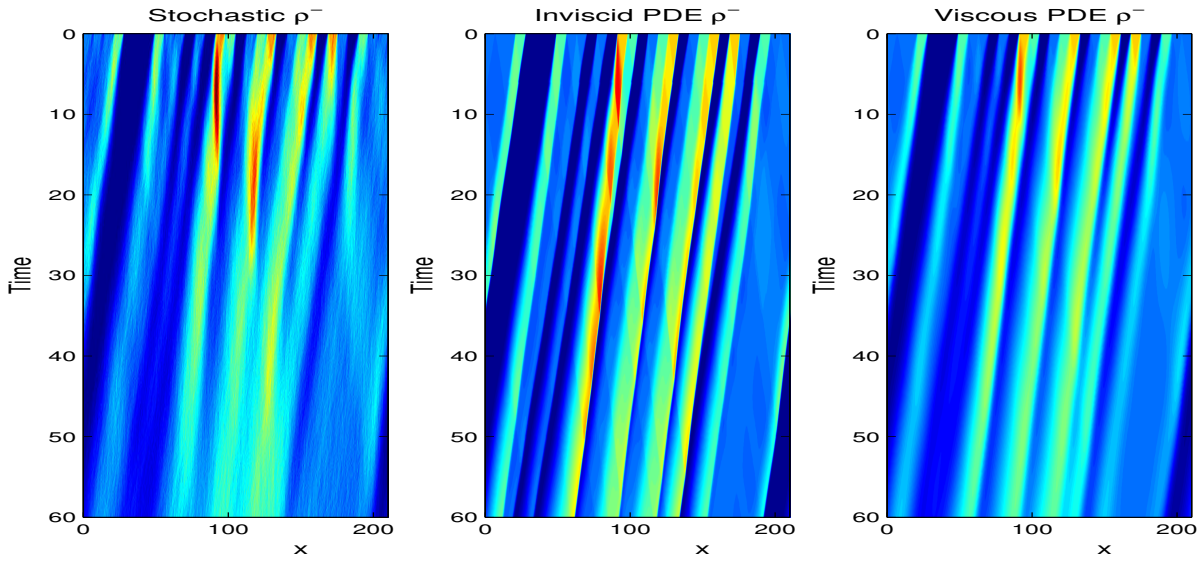
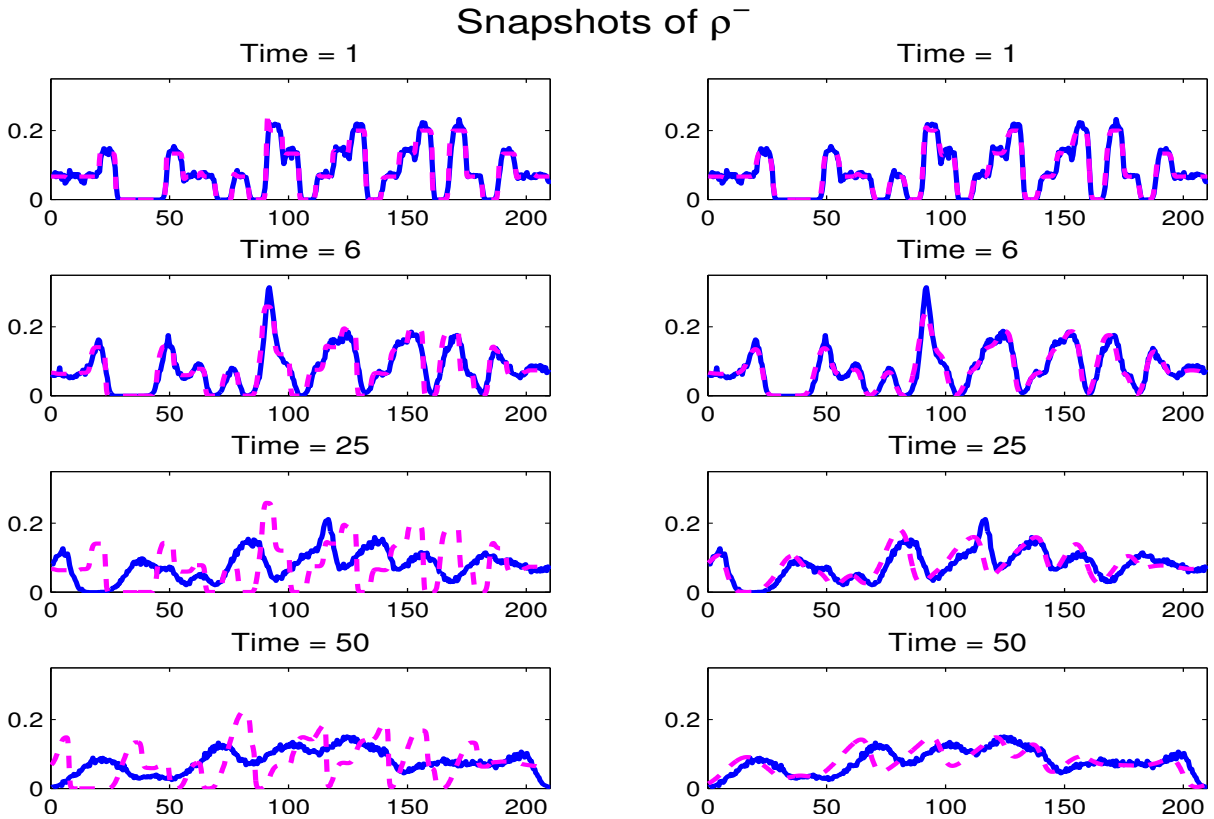Figure 5.9: The same as in Figure 5.7 but for left-moving pedestrians.

Figure 5.10: Time snapshots of the solution from Figure 5.8. The solid blue line represents the CA solution, while the dashed magenta line represents the inviscid (left) and viscous with $\varepsilon = 0.5$ (right) PDE solutions.

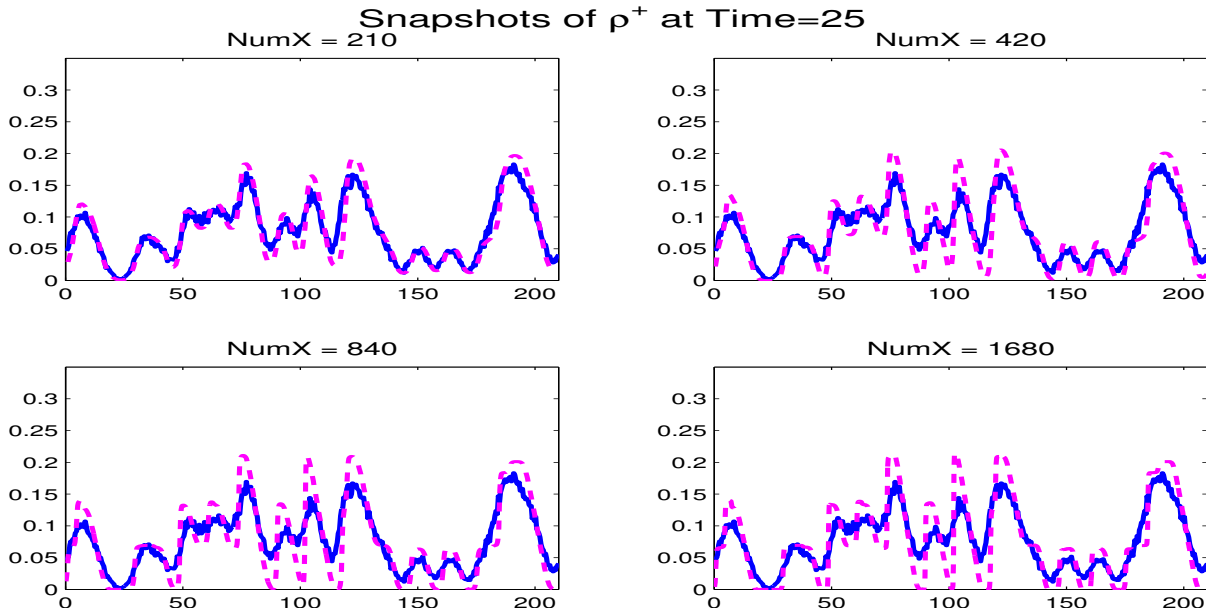hyperbolicity criterion is given by (4.9)).

Figure 5.11: Comparison of the snapshots of the solution at time $t = 25$ for different spatial resolutions. The solid blue line represents the CA solution, while the dashed magenta line represents the inviscid PDE solutions computed with different number of grid points in the mesh.

To illustrate the nonhyperbolic behavior we choose the velocities to be (5.6) with $a = 2$ and the initial density in the simulations of the coarse-grained PDE models to be

$$\rho^+(x, 0) = \begin{cases} 0.6, & 140 \le k \le 210, \\ 0, & \text{otherwise}, \end{cases} \qquad \rho^-(x, 0) = \begin{cases} 0.6, & 186.6 \le x \le 233.3, \\ 0, & \text{otherwise}, \end{cases} \qquad (5.7)$$

that is, the initial data are in the nonhyperbolic regime. The computational domain is $[0, 420]$ and the simulations are conducted on a $\Delta x = 420/1280$ grid.

The initial pedestrian distribution for the CA computations is sampled from the initial density (5.7). The number of cells in the stochastic simulations is $N = 900$, the cell size is $420/900 \approx 0.4667m$, the time step is $\Delta t = 0.005$ and $MC = 3000$.

Here, we depict only ρ^+ since ρ^- exhibits a similar behavior. Comparison between the stochastic and inviscid PDE simulations is shown in Figure 5.12. As one can see, the PDE solution develops spurious large magnitude oscillations, which demonstrates that the inviscid system (4.7) is ill-posed. Figure 5.13 shows ρ^+ computed using the viscous PDE model (4.10). The results suggest that the nonlinear diffusion present in (4.10) stabilizes the PDE solution: The bigger value of $\varepsilon = 1.5$ fully suppresses spurious oscillations and leads to a very good agreement between the CA and PDE simulations.

Remark 5.1 Since coarse-grained PDEs are discretized on a finite mesh with a particular mesh-size Δx numerical diffusion can affect simulations of both the systems (4.7) and (4.10). Numerical diffusion inversely proportional to the number of points in the mesh and can lead to significant numerical errors if the mesh size Δx is not sufficiently small (i.e. the use of coarser meshes typically leads to the increasing numerical diffusion). A particular example of numerical diffusion affecting the numerical solution is presented in Figure 5.11.
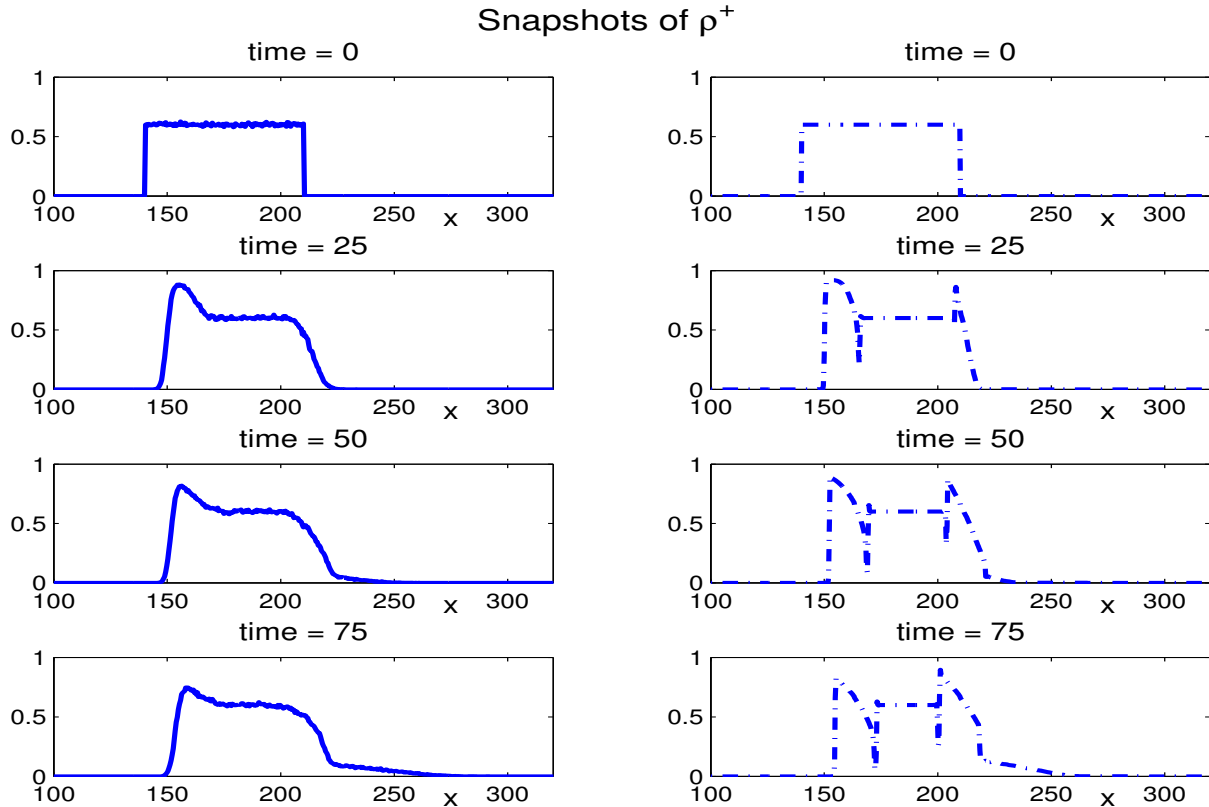
Figure 5.12: Densities of the right-moving pedestrians computed by the CA (left) and inviscid PDE (right) models with the initial conditions (5.7) and velocities (5.6) with $a = 2$.

We have verified that all of our numerical PDE simulations in Sections 5.1, 5.2, and 5.3 are not affected significantly by the grid refinement. In particular, we have refined the mesh and performed computations with $N = 700$ and $N = 1400$ in Section 5.1, with $N = 1680$ in Section 5.2, and with $N = 2560$ and $N = 5120$ in Section 5.3. We have not observed any noticeable changes in the numerical solution of the coarse-grained PDEs. Therefore, we conclude that the numerical diffusion is not significant in the simulations presented in this paper.

6 Conclusion

In this paper, we have developed a PDE formulation for the pedestrian dynamics in a narrow street or corridor. The resulting 1-D system of PDEs has been systematically derived from a microscopic stochastic CA model. The slowdown rules in the CA model need to be specified explicitly by prescribing different velocities when pedestrians moving in the opposite directions are present. The condition of approximate independence of neighboring cells is essential for the derivation of the coarse-grained PDE model and "propagate" into the macroscopic PDE formulation resulting in a particular form of the flux. We have also demonstrated that the resulting PDE is only conditionally hyperbolic. To stabilize the resulting PDE system we have rigorously derived the nonlinear diffusion correction using the intermediate mesoscopic model.

We have performed a number of numerical experiments comparing and contrasting the statis-
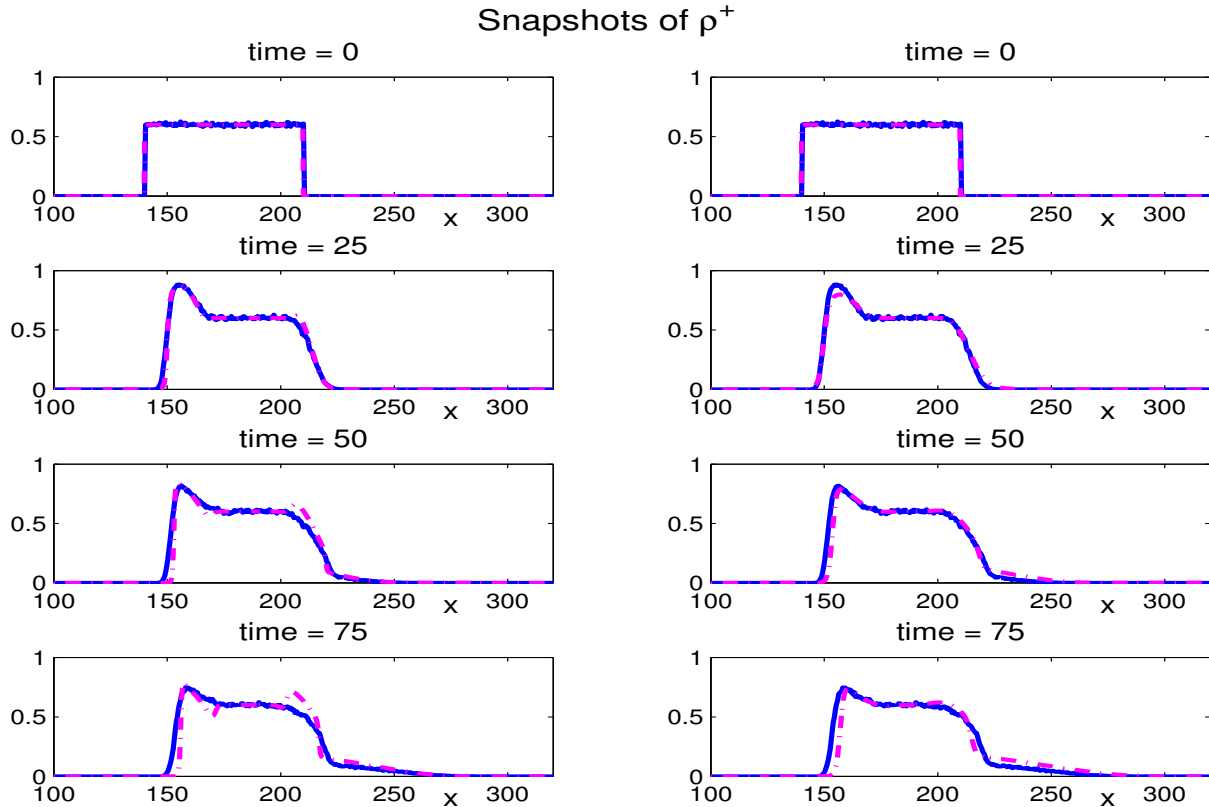
Figure 5.13: Densities of the right-moving pedestrians computed by the CA and viscous PDE models with the initial conditions (5.7) and velocities (5.6) with $a = 2$. The solid blue line represents the CA solution, while the dash-dotted magenta line represents viscous PDE solutions with $\varepsilon = 0.5$ (left) and $\varepsilon = 1.5$ (right).

tical behavior of the stochastic solution and its deterministic PDE counterparts. Our numerical experiments indicate that in the case of weak slowdown interactions, the average behavior of the stochastic CA model is reproduced quite well by the coarse-grained PDE model. On the other hand, the approximate independence assumption does not seem to hold in the case of the stronger slowdown regime, which results in a considerable discrepancy between the stochastic and deterministic results.

In addition, our numerical experiments indicate that the statistical behavior of the microscopic CA model is more diffusive than the corresponding deterministic inviscid coarse-grained analog. Therefore, we also derived the second-order diffusive correction of the coarse-grained PDE. We have numerically demonstrated that these nonlinear diffusive corrections lead to a significant improvement in reproducing the CA results using the PDE model. One of the possible aspects of future research includes fitting parameters of the stochastic model (e.g. velocities c_i) and, thus, fitting the parameters of the coarse-grained PDE using experimental data. Nevertheless, the nonlinear diffusive corrections derived in this paper have a rather general form and can be used in other models of bi-directional traffic.

We would also like to point out that the PDE simulations are an order of magnitude faster than the corresponding CA ones. Therefore, the coarse-grained PDE systems have considerable numerical advantages in practical applications such as real-time predictions of the pedestrian traffic

via filtering, investigation of pedestrian traffic flow on networks, etc. These and other issues will be investigated in subsequent papers.

A Central-Upwind Scheme for Systems of Conservation Laws

In this section, we briefly describe a semi-discrete second-order central-upwind scheme used for numerical solution of the 1-D systems (4.7) and (4.10), which can be written as

$$\boldsymbol{\rho}_t + \mathbf{F}(\boldsymbol{\rho})_x = (Q(\boldsymbol{\rho})\boldsymbol{\rho}_x)_x, \tag{A.1}$$

with $\boldsymbol{\rho} = (\rho^+, \rho^-)^T$, the flux $\mathbf{F}(\boldsymbol{\rho}) = \big(f(\rho^+)g(\rho^-), f(\rho^-)g(\rho^+)\big)^T$, and the viscosity matrix

$$Q(\boldsymbol{\rho}) = \frac{\varepsilon}{2} \begin{pmatrix} g(\rho^-) & (c_1 - c_2)f(\rho^+) \\ (c_1 - c_2)f(\rho^-) & g(\rho^+) \end{pmatrix}.$$

For simplicity, we divide the computational domain into finite-volume cells $C_j = [x_{j-\frac{1}{2}}, x_{j+\frac{1}{2}}]$ of a uniform size Δx with $x_j = j\Delta x$ and denote by

$$\overline{\boldsymbol{\rho}}_j(t) = \frac{1}{\Delta x} \int_{C_j} \boldsymbol{\rho}(x, t)\, dx,$$

the computed cell averages of the solution $\boldsymbol{\rho}$, which we assume to be available at time t. The semi-discrete central-upwind scheme for (A.1) is given by the following system of ODEs for $\overline{\boldsymbol{\rho}}_j$:

$$\frac{d\overline{\boldsymbol{\rho}}_j(t)}{dt} = -\frac{\mathbf{H}_{\mathbf{j}-\frac{1}{2}}(\mathbf{t}) - \mathbf{H}_{\mathbf{j}+\frac{1}{2}}(\mathbf{t})}{\Delta x} + \frac{\mathbf{P}_{\mathbf{j}-\frac{1}{2}}(\mathbf{t}) - \mathbf{P}_{\mathbf{j}+\frac{1}{2}}(\mathbf{t})}{\Delta x}, \tag{A.2}$$

where the numerical hyperbolic $\mathbf{H}_{\mathbf{j}+\frac{1}{2}}(\mathbf{t})$ and parabolic $\mathbf{P}_{\mathbf{j}+\frac{1}{2}}(\mathbf{t})$ fluxes are constructed as follows (for convenience, we will omit the dependence of the computed quantities on t in the rest of the text).

We first reconstruct a piecewise linear approximation,

$$\widetilde{\boldsymbol{\rho}}(x) = \overline{\boldsymbol{\rho}}_j + (\boldsymbol{\rho}_x)_j(x - x_j), \quad x \in C_j. \tag{A.3}$$

The numerical derivatives $(\boldsymbol{\rho}_x)_j$ should be computed componentwise and are (at least) first-order approximations of $\boldsymbol{\rho}_x(x_j, t)$, calculated using a nonlinear limiter needed to avoid oscillations in the

reconstruction (A.3). In our numerical experiments, we have used the generalized minmod limiter (see, e.g., [18, 20]):

$$(\boldsymbol{\rho}_x)_j = \text{minmod}\left(\theta\frac{\overline{\boldsymbol{\rho}}_j - \overline{\boldsymbol{\rho}}_{j-1}}{\Delta x}, \; \frac{\overline{\boldsymbol{\rho}}_{j+1} - \overline{\boldsymbol{\rho}}_{j-1}}{2\Delta x}, \; \theta\frac{\overline{\boldsymbol{\rho}}_{j+1} - \overline{\boldsymbol{\rho}}_j}{\Delta x}\right), \quad \theta \in [1, 2], \tag{A.4}$$

where the minmod function is defined as

$$\text{minmod}(z_1, z_2, ...) := \begin{cases} \min_j\{z_j\}, & \text{if } z_j > 0 \;\; \forall j, \\ \max_j\{z_j\}, & \text{if } z_j < 0 \;\; \forall j, \\ 0, & \text{otherwise,} \end{cases} \tag{A.5}$$

and the parameter θ can be used to control the amount of numerical viscosity present in the resulting scheme (larger values of θ correspond to less dissipative but, in general, more oscillatory reconstructions).

The reconstruction (A.3) is, in general, discontinuous at the cell interfaces, $x = x_{j+\frac{1}{2}}$, where it has two values, which we denote by

$$\boldsymbol{\rho}_j^{\text{E}} := \overline{\boldsymbol{\rho}}_j + \frac{\Delta x}{2}(\boldsymbol{\rho}_x)_j, \quad \boldsymbol{\rho}_j^{\text{W}} := \overline{\boldsymbol{\rho}}_j - \frac{\Delta x}{2}(\boldsymbol{\rho}_x)_j. \tag{A.6}$$

These discontinuities propagate in time with one-sided local speeds that can be estimated from the eigenvalues λ of the Jacobian matrix (4.8) and are calculated in the following way. We denote by

$$R = f'(\rho^+)g(\rho^-) - f'(\rho^-)g(\rho^+), \quad D = \left[f'(\rho^-)g(\rho^+) + f'(\rho^+)g(\rho^-)\right]^2 - 4f(\rho^-)f(\rho^+)g'(\rho^-)g'(\rho^+)$$

and consider two possible cases:

- If both $D_j^{\text{E}} \geq 0$ and $D_{j+1}^{\text{W}} \geq 0$ (hyperbolic regime), then

$$a_{j+\frac{1}{2}}^+ = \frac{1}{2}\max\left\{R_j^{\text{E}} + \sqrt{D_j^{\text{E}}}, \; R_{j+1}^{\text{W}} + \sqrt{D_{j+1}^{\text{W}}}, \; 0\right\},$$

$$a_{j+\frac{1}{2}}^- = \frac{1}{2}\min\left\{R_j^{\text{E}} - \sqrt{D_j^{\text{E}}}, \; R_{j+1}^{\text{W}} - \sqrt{D_{j+1}^{\text{W}}}, \; 0\right\},$$

- If either $D_j^{\text{E}} < 0$ or $D_{j+1}^{\text{W}} < 0$ (nonhyperbolic regime), then

$$a_{j+\frac{1}{2}}^+ = \frac{1}{2}\max\left\{\sqrt{(R_j^{\text{E}})^2 - D_j^{\text{E}}}, \; \sqrt{(R_{j+1}^{\text{W}})^2 - D_{j+1}^{\text{W}}}\right\},$$

$$a_{j+\frac{1}{2}}^- = -a_{j+\frac{1}{2}}^+.$$

The numerical fluxes are then given by

$$\mathbf{H_{j+\frac{1}{2}}} = \frac{a_{j+\frac{1}{2}}^+\mathbf{F}(\boldsymbol{\rho}_j^{\text{E}}) - a_{j+\frac{1}{2}}^-\mathbf{F}(\boldsymbol{\rho}_{j+1}^{\text{W}})}{a_{j+\frac{1}{2}}^+ - a_{j+\frac{1}{2}}^-} + \frac{a_{j+\frac{1}{2}}^+ a_{j+\frac{1}{2}}^-}{a_{j+\frac{1}{2}}^+ - a_{j+\frac{1}{2}}^-}\left[\boldsymbol{\rho}_{j+1}^{\text{W}} - \boldsymbol{\rho}_j^{\text{E}}\right],$$

$$\mathbf{P_{j+\frac{1}{2}}} = Q(\boldsymbol{\rho}_{j+\frac{1}{2}})\frac{\overline{\boldsymbol{\rho}}_{j+1} - \overline{\boldsymbol{\rho}}_j}{\Delta x}, \quad \boldsymbol{\rho}_{j+\frac{1}{2}} = \frac{\boldsymbol{\rho}_j^{\text{E}} + \boldsymbol{\rho}_{j+1}^{\text{W}}}{2}. \tag{A.7}$$

Finally, the resulting semi-discretization (A.2)–(A.7) is a time-dependent ODE system, which should be numerically integrated using a stable ODE solver of an appropriate order. In our numerical experiments we have used the third-order strong stability preserving Runge-Kutta method (see [10]).

Remark A.1 Notice that the choice of one-sided local speeds in the nonhyperbolic regime is ad-hoc. However, it is important to point out that we have not tried to stabilize the inviscid PDE solution by increasing the amount of numerical viscosity: The solution has been stabilized by adding nonlinear diffusion terms rigorously derived from the mesoscopic formulation.

References

[1] T. Alperovich and A. Sopasakis, *Modeling highway traffic with stochastic dynamics*, J.Stat.Phys, 133 (2008), pp. 1083–1105.

[2] C. Appert-Rolland, P. Degond, and S. Motsch, *Two-way multi-lane traffic model for pedestrians in corridors*, Networks and Heterogeneous Media, 6 (2011), pp. 351–381.

[3] N. Bellomo and C. Dogbe, *On the modelling crowd dynamics: from scaling to second order hyperbolic macroscopic models*, Math. Models Methods Appl. Sci., 18 (2008), pp. 1317–1345.

[4] ——, *On the modeling of traffic and crowds: A survey of models, speculations, and perspectives*, SIAM Review, 53 (2011), pp. 409–463.

[5] V. J. Blue and J. L. Adler, *Cellular automata microsimulation for modeling bi-directional pedestrian walkways*, Transportation Research Part B, 35 (2001), pp. 293–312.

[6] C. Burstedde, K. Klauck, A. Schadschneider, and J. Zittarz, *Simulation of pedestrian dynamics using a 2-dimensional cellular automaton*, Physica A, 295 (2001), pp. 507–525.

[7] A. Chertock, A. Kurganov, and A. Polizzi, *Multi-class traffic flow model with look-ahead dynamics*, Preprint, (2010).

[8] N. Dundon and A. Sopasakis, *Stochastic modeling and simulation of multi-lane traffic*, Transportation and Traffic Theory 2007: Papers selected for presentation at ISTTT17, (2007), pp. 661–691.

[9] M. Fukui and Y. Ishibashi, *Self-organized phase transitions in cellular automaton models for pedestrians*, J. Phys. Soc. Jpn., 68 (1999), pp. 2861–2863.

[10] S. Gottlieb, C.-W. Shu, and E. Tadmor, *Strong stability-preserving high-order time discretization methods*, SIAM Rev., 43 (2001), pp. 89–112.

[11] R. Y. Guo and H. J. Huang, *A mobile lattice gas model for simulating pedestrian evacuation*, Physica A, 387 (2008), pp. 580–586.

[12] C. Hauck, Y. Sun, and I. Timofeyev, *On cellular automata models of traffic flow with look-ahead potential*, arXiv:1209.5802, submitted to Stochastics and Dynamcis, (2013).

[13] D. Helbing, *A fluid dynamic model for the movement of pedestrians*, Complex Systems, 6 (1992), pp. 391–415.

[14] ──, *Traffic and related self-driven many-particle systems*, Rev. Mod. Phys., 73 (2001), pp. 1067–1141.

[15] D. Helbing and P. Molnar, *Social force model for pedestrian dynamics*, Physical Review E, 51 (1995), pp. 4282–4286.

[16] A. Kurganov and C.-T. Lin, *On the reduction of numerical dissipation in central-upwind schemes*, Commun. Comput. Phys., 2 (2007), pp. 141–163.

[17] A. Kurganov, S. Noelle, and G. Petrova, *Semi-discrete central-upwind scheme for hyperbolic conservation laws and Hamilton-Jacobi equations*, SIAM J. Sci. Comput., 23 (2001), pp. 707–740.

[18] K.-A. Lie and S. Noelle, *On the artificial compression method for second-order nonoscillatory central difference schemes for systems of conservation laws*, SIAM J. Sci. Comput., 24 (2003), pp. 1157–1174.

[19] M. Moussaïd, E. G. Guillot, M. Moreau, J. Fehrenbach, O. Chabiron, S. Lemercier, J. Pettré, C. Appert-Rolland, P. Degond, and G. Theraulaz, *Traffic instabilities in self-organized pedestrian crowds*, PLoS Comput. Biol., 8 (2012), p. e1002442.

[20] H. Nessyahu and E. Tadmor, *Nonoscillatory central differencing for hyperbolic conservation laws*, J. Comput. Phys., 87 (1990), pp. 408–463.

[21] A. Sopasakis and M. Katsoulakis, *Stochastic modeling and simulation of traffic flow: Asymmetric single exclusion process with arrhenius look-ahead dynamics*, SIAM J. Appl. Math., 66 (2006), pp. 921–944.

[22] G. C. K. Wong and S. C. Wong, *A multi-class traffic flow model – an extension of LWR model with heterogeneous drivers*, Transportation Research, 36A (2002), pp. 827–841.

[23] J. Zhang, W. Klingsch, A. Schadschneider, and A. Seyfried, *Ordering in bidirectional pedestrian flows and its influence on the fundamental diagram*, arXiv:1107.5246, (2011).

[24] J. Zhang and A. Seyfried, *Empirical characteristics of different types of pedestrian streams*, arXiv:1207.5931, (2012).